



Available online at www.sciencedirect.com
jmr&t
 Journal of Materials Research and Technology
 journal homepage: www.elsevier.com/locate/jmrt



Integrating experiments, finite element analysis, and interpretable machine learning to evaluate the auxetic response of 3D printed re-entrant metamaterials

Bolaji Oladipo ^a, Helio Matos ^b, N.M. Anoop Krishnan ^{c,d}, Sumanta Das ^{a,b,*}

^a Department of Civil and Environmental Engineering, University of Rhode Island, Kingston, RI, 02881, United States

^b Department of Mechanical, Industrial and Systems Engineering, University of Rhode Island, Kingston, RI, 02881, United States

^c Department of Civil Engineering, Indian Institute of Technology Delhi, Hauz Khas, New Delhi, 110016, India

^d Yardi School of Artificial Intelligence, Indian Institute of Technology Delhi, Hauz Khas, New Delhi, 110016, India

ARTICLE INFO

Article history:

Received 25 January 2023

Accepted 4 June 2023

Available online 10 June 2023

Keywords:

Machine learning

Neural network

Re-entrant

Auxetic behavior

SHAP

Finite element analysis

3D printing

ABSTRACT

Metamaterials have received extensive attention in fundamental and applied research over the past two decades due to their unique mechanical behavior. This paper presents an interpretable machine learning (ML) approach for efficient response prediction of three-dimensional (3D)-printed metamaterials. However, developing such an ML-based model requires a large consistent, representative, balanced, and complete dataset. To this extent, an experimentally validated finite element analysis (FEA) approach is implemented to generate 8096 non-self-intersecting re-entrant honeycomb structures by varying the mesoscale geometrical features to obtain the corresponding Poisson's ratios. This dataset is leveraged to develop a feed-forward multilayer perceptron-based predictive model. The developed ML model shows excellent predictive efficacy on the unseen test dataset. Shapely additive explanation (SHAP) is then used for model interpretation. SHAP results show that the slant cell length is the dominant input feature dictating the model output whereas cell angle and vertical cell length show mixed trends signifying that other input features influence their effect on the model output. Moreover, cell thickness does not significantly influence the model output when compared to other input features. Overall, the integrated numerical simulation-experiment-interpretable ML-based predictive approach presented here can be leveraged to design and develop metamaterials for a wide range of engineering applications.

© 2023 The Author(s). Published by Elsevier B.V. This is an open access article under the CC BY-NC-ND license (<http://creativecommons.org/licenses/by-nc-nd/4.0/>).

* Corresponding author.

E-mail address: sumanta_das@uri.edu (S. Das).

<https://doi.org/10.1016/j.jmrt.2023.06.038>

2238-7854/© 2023 The Author(s). Published by Elsevier B.V. This is an open access article under the CC BY-NC-ND license (<http://creativecommons.org/licenses/by-nc-nd/4.0/>).

1. Introduction

Additive manufacturing (AM), also known as three-dimensional (3D) printing, allows for the rapid prototyping of intricate geometries leading to efficient avenues for innovations in developing various mechanical metamaterials. Mechanical metamaterials that exhibit a negative Poisson's ratio are termed auxetics [1,2]. The negative Poisson's ratio implies that the material expands transversely under uniaxial tension and contracts under uniaxial compression [3,4]. The first human-made auxetic foam structure with a Poisson's ratio of -0.7 was created by Lakes in 1987 [5], where low-density foams of open-cell polymer were altered to protrude inward, causing them to take a re-entrant shape. More studies have since been conducted to increase the knowledge and awareness of mechanical metamaterials [6–10]. Due to the negative Poisson's ratio from the geometrical patterns of auxetic structures, desirable mechanical properties such as indentation and impact resistance [11], negative stiffness [12], ultrahigh stiffness [13], zero shear modulus [14], and fracture toughness [15] among other outstanding mechanical responses [16,17] in areas such as in biomedical engineering for bone scaffolding [18], defense for high energy-absorbing materials [19], textile fabric developments [20], furniture [21], and in smart devices [22] have been discovered. A wide range of geometries of the auxetic structure has been proposed in the literature. These geometries include re-entrant [23], bowtie-shaped [24], lozenge [25], rotating triangle [26], chiral [27], anti-tetrarchical [28], double arrow [29], rotating square and rectangle [30], star [31], S-structure [32], and the forms that are inspired through the Kirigami techniques [33,34]. Moreover, the so-called AUXHEX mechanical metamaterial has zero Poisson's ratio and was developed using a Kirigami-inspired design [35].

Auxetic metamaterials have been fabricated from a wide variety of materials, such as metals [36], ceramics [37], textiles [38], polymers and biopolymer gels [39]. Employing traditional manufacturing methods to fabricate auxetic structures poses a limitation in realizing geometries with desired structural properties without spending needless time and resources [40,41], especially on a large scale [42]. To ease these limitations of the traditional manufacturing methods, AM started gaining relevance [43] owing to the techniques' high design efficiency, less tendency of material wastage, and ability to produce complex geometries [44]. Fused filament fabrication (FFF) is an AM method that works by printing layers upon layers of polymer filament through an extruder with flexibility and ease of customization of printed parts [45,46] using a wide range of thermoplastics [47,48].

Additively manufactured structures have been used for applications that require low temperature, low modulus of elasticity [49], wear resistance, highly retractable [50], and strong and tough interlayer adhesion. Thermoplastic polyurethane (TPU), of all the available thermoplastic filaments, is a competitive option for several engineering applications [51,52], such as in piezoresistors for flexible conductive composites [53], medicine for bistable implants [54], composite blends for shape memory effects [55], and flame retardant for fire resistant cable jackets [56]. Recent advancements in the

manufacturing of negative Poisson's ratio materials have extended beyond traditional AM. Assembled mechanical metamaterials present a promising method for creating auxetic structures, as showcased by Lang et al. [57], who developed an assembled structure with tunable Poisson's ratios. Furthermore, Jiang et al. [58] introduced a fabrication methodology for auxetic structures based on assembly, circumventing the need for expensive techniques like 3D printing or laser cutting. This approach offers multi-stage densification and programmable stiffness, suitable for low-cost, large-scale fabrication. Lastly, Zhang et al. [59] proposed a novel, low-cost approach for manufacturing auxetic chiral honeycombs using crosswise assembly with slotted wave plates. These advancements in assembly-based fabrication techniques open new avenues for cost-effective and customizable manufacturing of auxetic structures. A crucial aspect in designing and developing these structures is the accurate assessment of Poisson's ratio, which plays a pivotal role in determining their unique, counter-intuitive deformation behavior [60–62].

As experiments and numerical simulation methods are being used, the computation time and power rise with structural complexity. In particular, the derivation of the Poisson's ratio for individual re-entrant honeycomb structures through experiments and numerical simulations can be arduous when working with thousands of geometric and other parametric variations, all of which are deterrents to large-scale design and utilization of these complex structures in a wide variety of practical engineering applications. It is thus imperative to develop user-friendly and efficient design tools so that requisite structural architectures can be efficiently tuned in these metamaterials to achieve desirable auxetic responses consistently. Therefore, this paper is fueled by the imminent need to develop a user-friendly and yet efficient design tool that explores the relationships between mesoscale architectural features of these re-entrant honeycomb metamaterials, and the resultant auxetic response to drive large-scale applications of these highly efficient structures across engineering disciplines for various emerging applications.

In this context, machine learning (ML) can serve as a computationally efficient and user-friendly alternative to complex finite element analysis (FEA)-based predictive tools [63–65]. As such, these ML-based tools can be easily leveraged by the designers and decision-makers which can potentially contribute toward reliable performance standard development as well as accelerate the acceptance of the re-entrant auxetic metamaterials in the mainstream for a wide range of applications. However, a sufficiently large dataset is required for accurately modeling ML algorithms [66,67], which is currently not readily available. To address this, in this paper, a large dataset is generated using experimentally validated FEA to provide a time-efficient method for evaluation. The large dataset of Poisson's ratios is created by extensively varying the geometric features of reentrant honeycombs. The key geometric features identified from the literature [68–71] include slant cell length, vertical cell length, cell angle, and cell thickness. These features are selected as they have been shown to play a crucial role in determining the Poisson's ratio of reentrant honeycomb structures. The dataset is leveraged to develop a neural network (NN)-based predictive approach

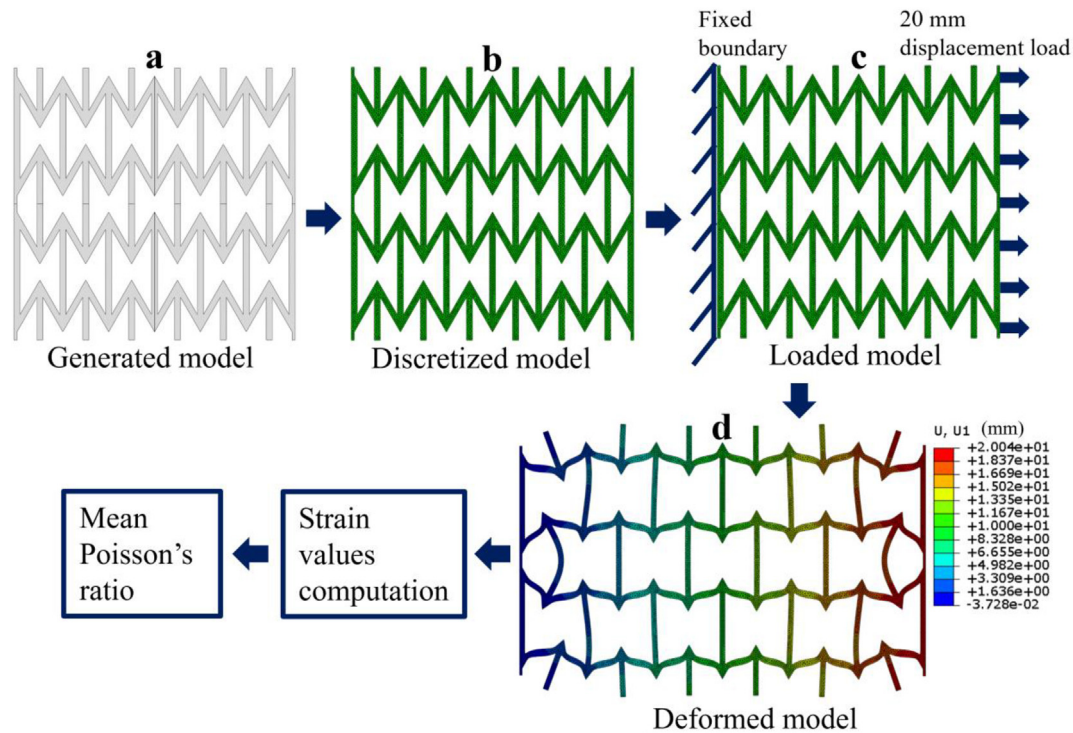


Fig. 1 – Schematic representation of the FEA simulation framework. From left to right, (a) the model generated from the Python script followed by (b) the TRI/QUAD discretized model, (c) the loaded model, and (d) the deformed model of the FEA with a color spectrum showing the maximum displacement tensile load of 20 mm.

to determine the Poisson's ratio of re-entrant honeycomb structures of TPU with different geometric features. Also, to interpret the predicted results, we employ Shapley additive explanation (SHAP), which reveals various design trends and provides valuable insights on the relative sensitivity of geometrical input features toward predicted auxetic response. The synergistic integration of FEA, experiments, and interpretable ML toward the development of efficient materials design tools based on mesoscale architectural descriptors is expected to enable engineers and materials designers to make intelligent, informed decisions regarding the selection of these re-entrant auxetic structures and thus accelerate their acceptance and mainstream utilization for various unexplored and emerging engineering applications.

2. Computational and experimental methods

2.1. Finite element analysis (FEA)

Abaqus CAE 2020 is utilized to evaluate the mechanical property of the Python script-generated sample structures using FEA. Fig. 1 shows the representative simulation framework. Fig. 1 (a) and (b) show the generated model and the discretized version of the geometry, respectively. In Fig. 1c, the generated auxetic structure has an applied 20 mm displacement in tension. The quadrilateral-dominant mesh of element type CPE4H [72] is used in discretizing the models.

Based on this uniform seed size, a curvature control is applied in a way as to make the small regions of big curvature properly approximate the mesh. Fig. 1d shows the deformed geometry under the applied loading. MATLAB-based post-processing module is utilized to compute the strains and Poisson's ratios. More details on different components of the simulation framework are provided in the subsequent sub-sections.

2.1.1. Geometry generation

For initial simulation and experimental validation, a geometry with a 20 mm vertical cell length, 15 mm slant cell length, 3 mm cell thickness, and 70° cell angle is generated using the Python script, which is provided in section D of the supplementary material [65]. The geometry is provided in Fig. S1 of the supplementary material. The TPU material properties specified in the Python script had a density of 1122 kg/m³, modulus of elasticity of 51 MPa, and Poisson's ratio of 0.48 [66]. Fig. 2 shows the Python script-generated 3D auxetic geometry. The figure also shows the details of the geometrical features of the geometry's unit cell, where h is the vertical cell length, l is the slant cell length, t is the cell thickness and θ is the cell angle. The thickness of the geometry in the z -direction is kept constant since it does not influence the Poisson's ratio of the structure in the x - y plane, when evaluated uniaxially.

2.1.2. Boundary conditions and deformation computation

The auxetic structure was subjected to uniaxial tension within the elastic region of the TPU material. Dirichlet boundary condition is set on the structure. One end of the structure is

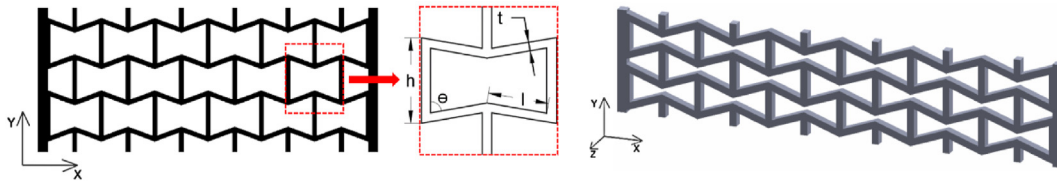


Fig. 2 – The geometry of the auxetic structure: a 3D model generated from the Python script and an elaborated section showing the unit cell geometrical features.

constrained to zero displacements in all directions, leaving the opposite end to bear the quasi-static unidirectional displacement load. The remaining two opposite sides are left free. The result of the deformation from the 20 mm displacement load is shown in Fig. 1d. The red region in Fig. 1d is the area on the structure with the maximum deformation from the tensile load. The Poisson's ratio was computed from the transverse and longitudinal displacements relative to their initial positions. Sample Abaqus files for FEA are publicly available in Ref. [73].

2.2. Experimental method

The auxetic structures are generated from the Python script, which is provided in section D of the supplementary material. The generated STL files are leveraged to print the samples using the Creality CR-10 V3 3D printer that utilizes the FFF method with Overture™ plastic filament (TPU batch number: 2102250186). The filament is printed at a print head temperature of 225 °C and bed temperature of 50 °C with a print speed of 30 mm/s at 100% infill to ensure consistent print results. The 3D printed parts with the geometry from Section 2.1.1 are painted with high-contrast speckles of equal ratios of black and white [74] and speckles diameter of less than 1 mm. The speckled surfaces produced a resolution of approximately 3 X 3 pixels, as inspected on the image post-processing software. The parts are tested on a 10 kN Shimadzu Autograph AGS-X Series universal tensile test machine (UTM) with a uniaxial displacement of 20 mm. The tensile tests are conducted and coupled with digital image correlation (DIC) method [68–70] within the elastic limit of the material at a speed of 2 mm/min and room temperature (RT = 25 °C).

During the tensile test, as shown in Fig. 3, images of the three deformed 3D printed parts are captured using FLIR BFS-U3-50S5M – C USB 3.1 Blackfly® S, Monochrome Camera at one frame per second. A total of 596 images are captured. The captured Tiff image files are imported into Correlated Solution's VIC 2D DIC software [75] to analyze the full-field displacements and strains.

Strain values both on the transverse axis ($\epsilon(T)$) and the longitudinal axis ($\epsilon(L)$) are computed, and the Poisson ratio (ν) was evaluated using Eq. (1). The 2D DIC technique was calibrated using the standard approach as mentioned in the VIC-2D user manual [76]. The calibration process involves simple mouse-clicking on the two opposite diagonal corner features and entering the known distance between the two corner features into the VIC-2D software. The software, thus, determines a scale to map pixels to the displacements.

$$\nu = \frac{-\epsilon(T)}{\epsilon(L)} \quad (1)$$

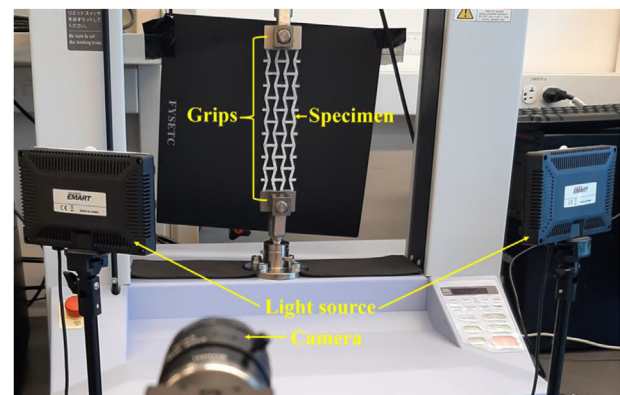
2.3. Computational and experimental results

The Poisson's ratio from the FEA simulations was compared to the tensile data. Fig. 4 (a)-(e) show the displacement images from the progression of the deformation. The undeformed image of the structure is shown in Fig. 4a followed by the subsequent deformation history up to the maximum 20 mm displacement in Fig. 4e. The Poisson's ratio evaluated from the three structures with the same geometrical features is -0.367 .

For the tensile test/DIC experiment, the entire face of the 3D printed structures, excluding the gripped ends, is selected as the area of interest, as illustrated in Fig. 5a. This selection enables the DIC to compute the strain values to include all the points on the features of the auxetic structures. Fig. 5b–(d) show how the auxetic structure increases in dimension transversely with applied uniaxial tension at 5, 10, and 17 mm, respectively. Fig. 5e shows the RT deformed structure at the maximum uniaxial displacement load of 20 mm. The Poisson's ratio evaluated from three replicate structures with the same geometrical features is -0.372 ± 0.006 , which correlates very well with the simulated value. The computational and testing data agree with each other. Hence the simulations are expanded to generate a large dataset to enable machine learning-based performance prediction.

3. Machine learning implementation

The ML model is developed using a multilayer perceptron (MLP). A single layer of the MLP [77] is represented by equation:



Figs. 3 – 2D DIC setup of a selected sample geometry.

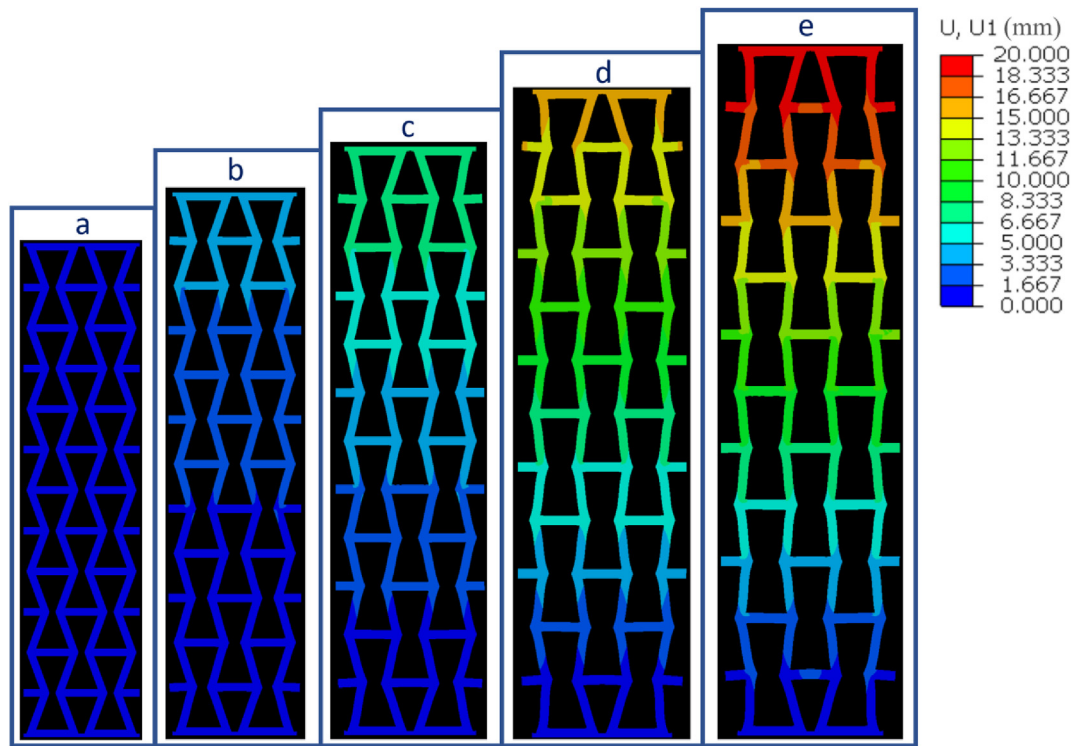


Fig. 4 – Computer numerical simulation images of the selected geometry showing (a) an undeformed shape, (b) 4 mm displacement load, (c) 10 mm displacement load, (d) 16 mm displacement load, (e) and 20 mm displacement load.

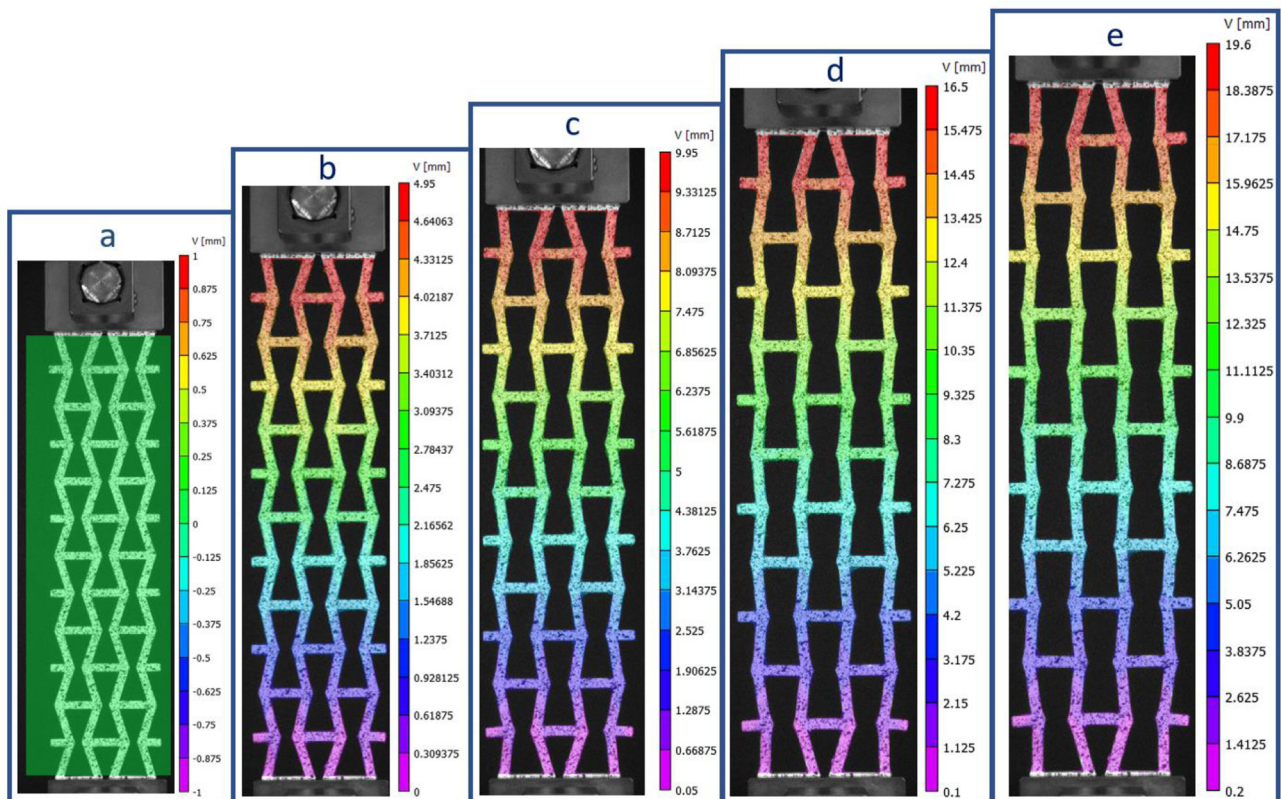


Fig. 5 – DIC images of the selected geometry showing (a) region of interest, (b) deformed sample at 5 mm displacement load, (c) 10 mm displacement load, (d) 17 mm displacement load, and (e) 20 mm displacement load.

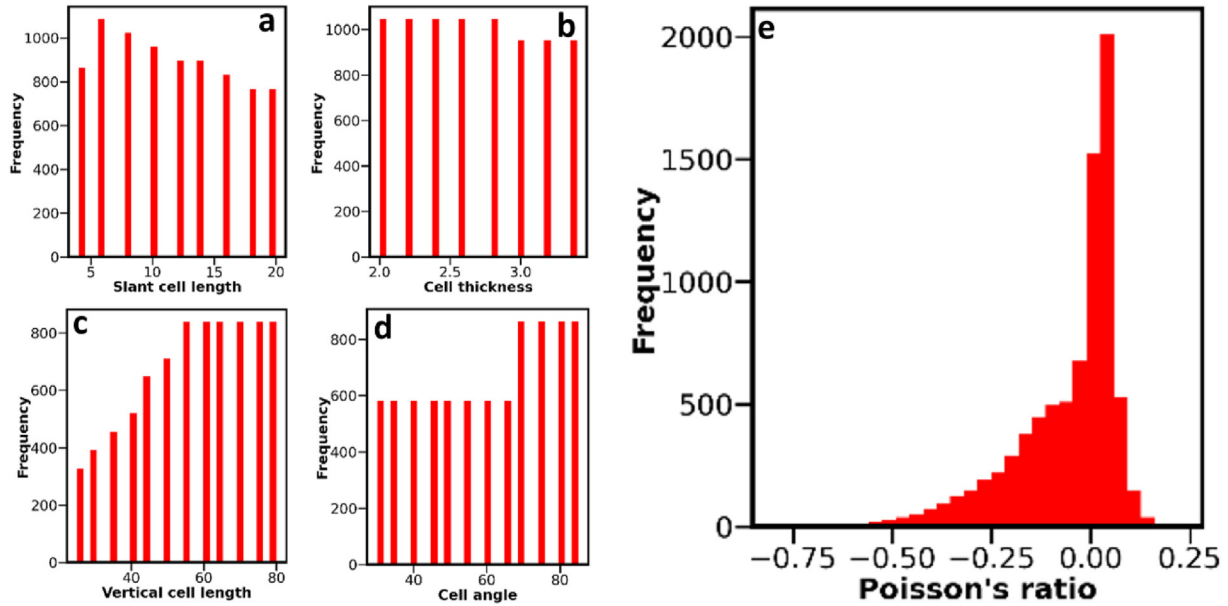


Fig. 6 – Dataset distribution of the independent features; (a) slant cell length, (b) cell thickness, (c) vertical cell length, (d) cell angle, and the dependent feature; (e) Poisson's ratio.

$$Y = f(W^T X + b) \quad (2)$$

where $X = (x_1, x_2, \dots, x_n)$ represent the n independent input features, Y represents the output label or value, W and b are the learnable weights and biases, respectively, and f is the activation function. Note that the specific architecture of an MLP can have multiple of such layers, with each layer having a number of hidden layer units. These form the hyperparameters of the model that need to be fixed prior to training the model. On the contrary, the weights and biases are the parameters of the model that are learned during the training of the model. The activation functions induce non-linearity to the otherwise linear MLPs. In the present work, all the activation functions are chosen as rectified linear unit (ReLU). ReLU, a non-smooth function was used in this study due to the computational efficiency it generates for an NN [78]. To learn the weights and biases, first, the MLP is initialized with a random assignment of weights and biases. Based on the loss function, backpropagation is employed to update the weight and biases to identify their optimal values that minimize the loss. The additional hyperparameters during the learning include the optimizer and the learning rate. In the present work, Adam is chosen as the optimizer [79]. The loss function chosen is the mean square error (MSE), where low MSE values indicate that the model has satisfactory performance. Below is Eq. (3) used to evaluate the MSE of the individual dataset.

$$MSE = \frac{1}{n} \sum_{i=1}^n [Y_i - \hat{Y}_i]^2 \quad (3)$$

where n is the batch size or the number of data points, Y_i is the measured Poisson's ratio, and \hat{Y}_i is the predicted Poisson's ratio by the MLP. In addition to MSE, R-squared (R^2) values are also used as an additional error metric.

3.1. Dataset generation and adequacy

Python scripts containing nested loops of the four geometrical features are loaded in batches into Abaqus CAE scripting to generate 8096 non-self-intersecting re-entrant honeycomb geometries. Each auxetic structure has a uniform re-entrant honeycomb pattern with six repeating units in the horizontal direction and three in the vertical direction. Fig. 6 shows the distribution of datasets of the independent features; (a) slant cell length, (b) cell thickness, (c) vertical cell length in millimeters, and (d) cell angle in degrees, and the dependent feature; (e) Poisson's ratio. To ensure adequacy, four important factors are carefully considered: (a) representativeness, (b) consistency, (c) completeness, and (d) the balanced nature of the dataset.

To ensure representativeness, careful consideration was made so that the dataset contains adequate information for training the model. Toward this, 20% of the whole dataset chosen randomly was kept unseen/hidden, and the remaining 80% data was used for training. Besides, 5-fold cross-validation was performed to tune the hyperparameters where during each fold, the dataset was further split into an 80% training set and a 20% validation set. Finally, the model was evaluated on the test set to determine the generalizability of unseen input features.

For the completeness and balanced nature of the dataset, all possible combinations of the independent features of the structures were considered in nested loops from the least possible values that yielded non-self-intersecting structures. These values were scaled up uniformly, choosing small step sizes, as illustrated in Table S1 of the supplementary material. For example, for the generation of geometries, the minimum slant cell length is 4 mm, and the minimum cell angle of 30° is

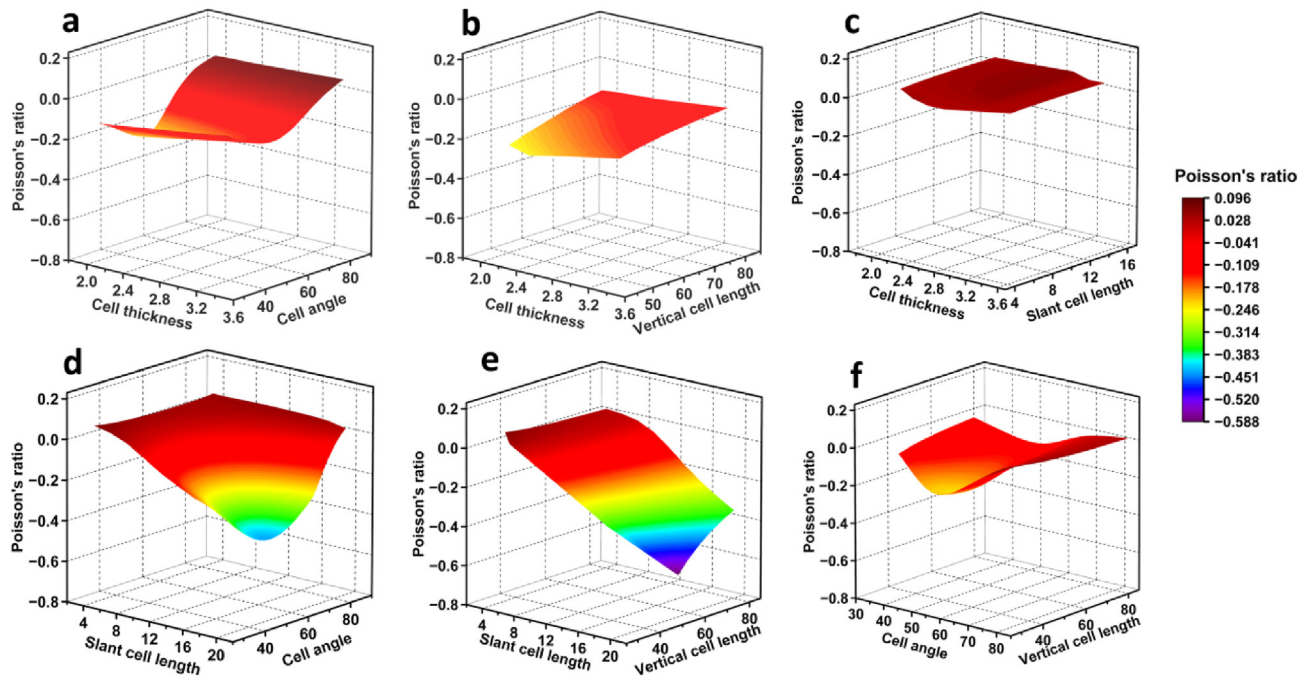


Fig. 7 – Influence of parametric interactions on the Poisson's ratio prediction: (a) cell thickness-cell angle interaction with slant cell length constant at 12 mm and vertical cell length at 50 mm (b) cell thickness-vertical cell length interaction with constant slant cell length of 12 mm and cell angle of 55°, (c) cell thickness-slant cell thickness interaction with constant vertical cell length of 50 mm and cell angle of 55°, (d) slant cell length-cell angle interaction with constant vertical cell length of 50 mm and cell thickness of 2.6 mm, (e) cell angle-vertical cell length interaction with cell thickness and cell angle constant at 2.6 mm and 55° respectively, and (f) slant cell length-vertical cell length interaction for a constant slant cell length of 12 mm and the cell thickness of 2.6 mm.

adopted. Any angle less than 30° at a step size of 5°, when combined with a slant cell length less than 4 mm created a self-intersecting structure. The step size of the slant cell length is 2 mm. For the cell thickness, the minimum cell thickness is 2.0 mm, and step size is 0.2 mm. Cell thicknesses less than 2.0 mm, combined with other geometrical features of any value, created zero thickness element mesh errors for the quadrilateral dominant mesh with the configurations used. The minimum vertical cell length is 25 mm at a step size of 5 mm, for all minimum allowable values for the other three geometrical features. The maximum vertical cell length, slant cell length, cell thickness, and cell angle are 80, 20, 3.4 mm, and 85°, respectively.

The 8096 different generated structures were each simulated for their Poisson's ratio, following an applied uniaxial displacement load. Fig. 1 shows a schematic illustration of the FEA framework. The numerical simulation of re-entrant honeycomb structures demonstrated that some auxetic structure geometries exhibit a positive Poisson's ratio. 49% of the Poisson's ratios evaluated were equal to or greater than zero, while 51% of the Poisson's ratios evaluated were less than zero. The highest Poisson's ratio of the auxetic structure geometries recorded is 0.23, while the lowest is -0.80. The plots of each geometrical feature versus the Poisson's ratios are provided in Fig. S2 of the supplementary material.

For a detailed evaluation of the generated dataset, the influence of the four geometrical features on the predicted

Poisson's ratios is explained in Fig. 7a-f) using surface plots. In Fig. 7a, keeping the slant cell length constant at 12 mm and vertical cell length at 50 mm, the Poisson's ratio decreased from 0.06 to -0.26 when the cell angle was reduced from 80 to 50°. However, the trend reverses beyond 50°, and the Poisson's ratio increases to -0.03 as the angle approaches 30°. The lowest Poisson's ratio of -0.26 was obtained for a cell thickness of 2.0 mm. At a constant slant cell length of 12 mm and cell angle of 55° in Fig. 7b, the Poisson's ratio increased with an increase in cell thickness from 2.0 to 3.4 mm, and an increase in vertical cell length from 45 to 80 mm.

The Poisson's ratios are not significantly affected by the cell thickness and slant cell length, as it can be seen in Fig. 7c. At a constant vertical cell length of 50 mm and cell angle of 55°, the Poisson ratio hovered from 0.03 to 0.06, as the cell thickness decreased from 3.0 to 2.0 mm. The least Poisson's ratio is recorded at a slant cell length of 4 mm. In Fig. 7d, the vertical cell length is pegged at 50 mm, and cell thickness is kept constant at 2.6 mm, whereas the slant cell length and angle varied. As it can be seen in Fig. 7d, Poisson's ratio remains unaffected by the variations in the cell angle for lower slant cell length values. However, at higher slant cell length values (beyond 16 mm), the Poisson's ratio significantly decreases as the cell angle is reduced from 80 to 50°.

The slant cell length and the vertical cell length are varied while keeping the cell thickness and cell angle constant at 2.6 mm and 55° in Fig. 7e and d, respectively. Here, the

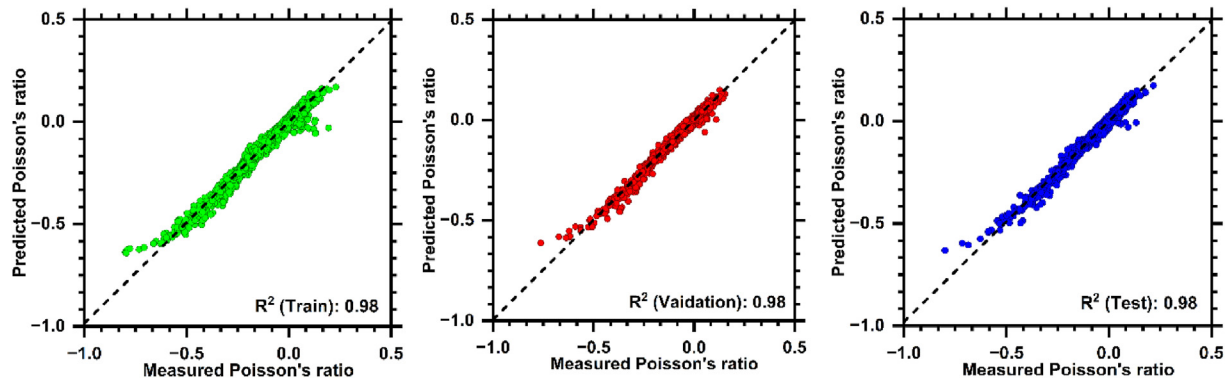


Fig. 8 – Comparison of the measured Poisson's ratio from the FEA model with the predicted Poisson's ratio from the trained NN model using (a) train set, (b) validation set, and (c) test set of data.

Poisson's ratio decreases from 0.10 to -0.59 as the slant cell length increases from 4 to 20 mm, while the vertical cell length of 55 mm shows the lowest Poisson's ratio of -0.59 . Fig. S3 in the supplementary material shows a heatmap that illustrates that slant cell length and vertical cell length have the strongest positive correlation. Keeping the slant cell length constant at 12 mm and the cell thickness at 2.6 mm (Fig. 5f), the Poisson's ratio decreases from 0.10 to -0.23 , as the cell angle is reduced from 80° to 50° but increases to -0.05 as the angle is reduced beyond 50° towards 30° . The vertical cell length shows a relatively lower influence on the predicted Poisson's ratios. Overall, slant cell length-cell angle and slant cell length-vertical cell length interactions significantly influence the negative Poisson's ratios compared to other parametric interactions, which are further explored later in this paper using interpretable machine learning.

3.2. Machine learning model

Tensorflow [80] ML system with Python is used for training the NN, due to its ability to run on multicore CPU and GPU. Optimization of the weights and the biases is accomplished by determining the model's loss function using the Adam algorithm through backpropagation. In order to optimize the performance of the NN model in this study, a thorough hyperparameter tuning process was considered. This involved carefully considering several hyperparameters, including the learning rate, number of epochs, number of hidden layers, and number of hidden nodes in each layer. MSE and R^2 values were employed to inform the selection of the optimum hyperparameters while balancing computational resources and model efficiency. A more detailed analysis of this process, including the selection of the optimum hyperparameters, is presented in section B of the supplementary material. The hyperparameter tuning process identified five neurons as the most efficient choice to balance model accuracy and computational resources. This conclusion was supported by the MSE and R^2 plots, as shown in the supplementary material (Fig. S4) for two hidden layers. Furthermore, a learning rate of 0.001 was obtained based on the learning rate sensitivity study as reported in the supplementary material (Figs. S5 and S6, and Table S2). Overall, after the tuning process, we obtained the

optimal hyperparameters for our model, which include a learning rate of 0.001, number of epochs of 200, number of hidden layers of 2, and number of neurons of 5. Such a hyperparameter tuning process helps to optimize the performance of the NN model and enables accurate predictions while minimizing computational resources.

The first operation that is conducted on the datasets to prevent overfitting is splitting the dataset into training datasets, and test datasets using Scikit learn library [81] in the ratio of 80:20. The 20% test dataset is kept hidden from the model during training, leaving the 80% only to be exposed and used for model training. At the end of the training, the hidden test dataset is revealed to evaluate the performance of the NN model. The model is trained with k-fold cross-validation (CV) [82]. The R^2 and MSE values deduced from each fold of the CV operation are averaged to evaluate the performance of the NN algorithm. A 5-fold CV on the training dataset enabled the dataset to be reshuffled to a dataset of 80% training and 20% validation [83]. The optimized neural network is provided in section C of the supplementary material.

3.3. Machine learning results

3.3.1. Predicted results

The performance of the NN model is determined by comparing the FEA-measured Poisson's ratios with the predicted Poisson's ratios data for the training, validation, and test datasets in Fig. 8. The R^2 values for the train, validation, and test datasets is 0.98.

3.3.2. SHAP interpretation of the predictions

In this section, the SHAP analysis is presented to provide more insight into the predicted Poisson's ratio and to clarify the relative importance of the slant cell length, cell angle, vertical cell length, and cell thickness. SHAP regression values are computed on all the simplified input features x' where x is the corresponding original input and f is the original model. $|z'|$ is the number of all the non-zero entries in z' , $z' \subseteq x'$ are all vectors of z' of simplified input features x' , and M is the number of features in the model. For all inputs $z' \in \{0, 1\}^M$, then the importance of feature i is given by $\phi_i(f, x)$ as shown in Eq. (4) [84].

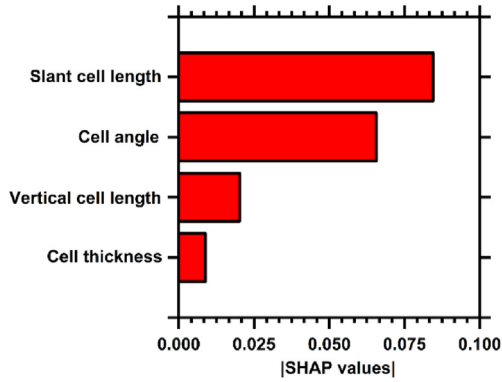


Fig. 9 – SHAP summary plot for the Poisson's ratio for each input from the trained NN model.

$$\varphi_i(f, x) = \sum_{z' \subseteq x} \frac{|z'|!(M - |z'| - 1)!}{M!} [f_x(z') - f_x(z' \setminus i)] \quad (4)$$

The relevance of the individual input features and the influence on the output feature are addressed by assigned importance values. Slant cell length and cell angle strongly influence the prediction of Poisson's ratios relative to the vertical cell length and the cell thickness. As it can be seen in Fig. 9, the Poisson's ratio prediction is dominated by the slant cell length with an absolute SHAP value of 0.08, followed by the cell angle with a SHAP value of 0.07, the vertical cell length with a SHAP value of 0.02, and the cell thickness with a SHAP value of 0.01.

To elucidate more on the relative importance of the input features, Fig. 10 shows the violin plots of the SHAP values for the individual input features that contributed to the prediction of the Poisson's ratios. The color scale from blue to red shows the range of values of the individual input feature, and the horizontal axis shows the SHAP values. While the red color represents the highest input feature value, the blue color represents the lowest value of the input feature. The mean Poisson's ratio of the entire datasets at -0.06 is represented by a SHAP value of zero. The features from top-down are arranged in descending order of importance.

Blue cluster toward the positive SHAP value axis of the slant cell length indicates that the SHAP values corresponding to Poisson's ratios greater than -0.06 correlate to low slant cell length values. A mix of a blue and red cluster from 0 to -0.2 SHAP values depicts that a mix of low and high slant cell length values correspond to the Poisson's ratios less than

-0.06 . SHAP values from -0.2 to -0.4 with the bold red line indicate that further negative Poisson's ratios less than -0.06 correlate to high slant cell length values. The observed relationship between slant cell length and Poisson's ratios, as revealed by our SHAP analysis, is consistent with trends derived from FEA as presented in Fig. 7 (please refer to Supplementary Fig. S7(a) for more details), where increased slant cell length corresponds to decreased Poisson's ratio values and vice versa. The red cluster from -0.07 to 0.28 on the cell angle SHAP violin shows that a small portion of the Poisson's ratio less than -0.06 and a large portion greater than -0.06 was predicted by high cell angle values. An inconsistent mix of red and blue clusters from -0.07 to -0.25 SHAP value depicts that a mix of low and high cell angle values predicted some negative Poisson's ratios. This observed mixed trend in case of cell angle aligns with FEA findings in Fig. 7 (please refer to Supplementary Fig. S7(b) for more details), which demonstrates that identical Poisson's ratio values can be obtained for two distinct cell angles even when all other geometrical features remain constant. This can be attributed to the due to highly nonlinear nature of the relationship between cell angle and Poisson's ratio as it can be observed in Fig. 7.

Red clusters from -0.03 to 0.1 SHAP values on the vertical cell length indicate that the quantity of Poisson's ratio from slightly below -0.06 up to the Poisson's ratios that correspond to the SHAP value of 0.1 was predicted by high vertical cell length values. From -0.03 to -0.07 SHAP values, the mix of blue and red indicates that a mix of low and high vertical cell length values predicted the corresponding Poisson's ratios below -0.06 . From -0.07 to -0.18 SHAP values on the vertical cell length, the blue clusters depict that low vertical cell length values predicted the negative Poisson's ratios in the cluster. The observed relationship between Poisson's ratio and vertical cell length corresponds well to the FEA trends depicted in Fig. 7 (see Supplementary Fig. S7(c) for further details), illustrating that smaller vertical cell length values are associated with lower Poisson's ratio values.

Cell thickness is a feature that has contributed the least to the prediction of Poisson's ratios. All the SHAP values are within the weak negative correlation of -0.1 and weak positive correlation of 0.1 . A cluster of Poisson's ratios is observed corresponding to a SHAP value of zero, and these mean Poisson's ratios around -0.06 are obtained for higher cell thickness values. In fact, most high cell thickness values yield Poisson's ratios equal to or higher than -0.06 . However, Poisson's ratios lower than -0.06 are also observed for higher cell thickness values. Results in Fig. 6 corresponding to cell

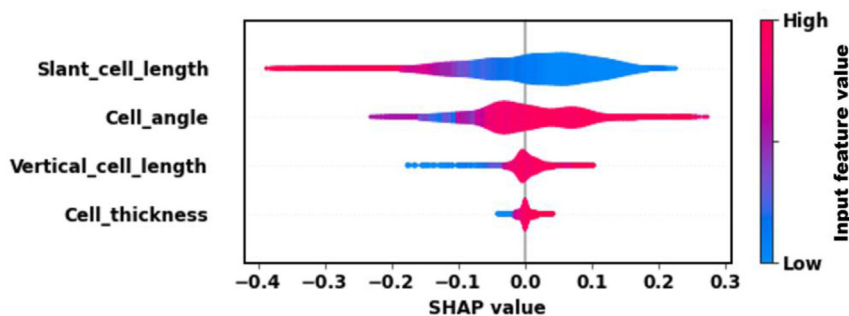


Fig. 10 – SHAP violin plot for the Poisson's ratio using the trained NN model.

thickness also indicate that lower cell thickness values always yield negative Poisson's ratios lower than -0.06 . The cell thickness-Poisson's ratio trend derived from our SHAP interpretation is in agreement with the FEA trends presented in Fig. 7 (refer to Supplementary Fig. S7(d) for additional details), indicating that an increase in cell thickness corresponds to an increase in Poisson's ratio. Hence, although cell thickness shows the least SHAP value (Fig. 9), the violin plot depicts that a judicious selection of lower cell thickness in the design of re-entrant honeycomb structures can provide substantial means to obtain an auxetic response. Overall, comparison of the SHAP violin plot trends and FEA trends reveals a generally good alignment between the two, indicating that the SHAP interpretations are consistent with the fundamental laws of physics. This observation highlights that the interpretable ML model, developed using a dataset generated through fundamental physics-based FEA, not only achieves outstanding predictive efficacy but also maintains the integrity of the underlying fundamental physics.

While the SHAP violin plot concentrates on the impact of a selected individual input feature on the prediction of the Poisson's ratios, the SHAP river flow plot, shown in Fig. 11, concentrates on the impact of the different input features on a selected Poisson's ratio [85]. The SHAP river flow plot of the NN model is illustrated in Fig. 11 for the individual Poisson's ratios, as the four input features influence them. Here, the expected value of -0.06 , indicates that the predicted value from the model would be the mean of all the 8096 Poisson's ratios in the training of the NN model when no information on the input feature values is available. Every line of the SHAP river flow plot corresponds to a specific Poisson's ratio. The tendency of these Poisson's ratio lines to sway above or below the expected value line is influenced by the value of the input feature in the model. The color spectrum corresponds to the property value for a given data point. While the red color represents low Poisson's ratio configuration, the blue represents high Poisson's ratio cases. Each predicted Poisson's ratio

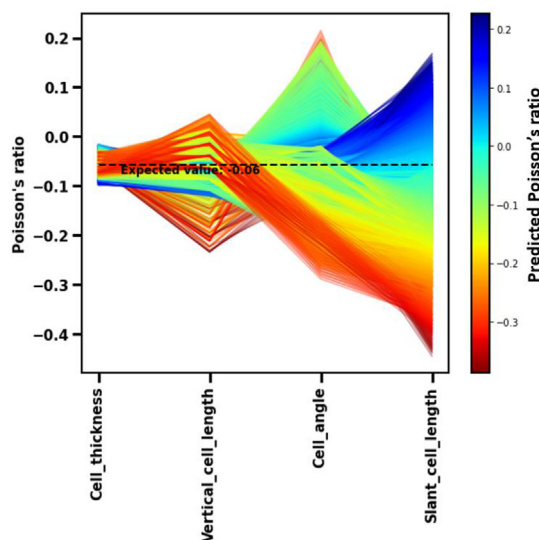


Fig. 11 – SHAP river flow plot for Poisson's ratio using the trained NN model.

progressed through the effect of the input features as indicated on the Poisson's ratio axis on the left side of the plot.

The order of arrangement of the input features from right to left on the horizontal axis is in decreasing absolute SHAP values. Fig. 11 shows a clear trend for the slant cell length. The slant cell length decreases the model predictions for low Poisson's ratio configurations. On the other hand, for high Poisson's ratio cases, the slant cell length increases the model predictions. Observation of such a clear trend signifies that slant cell length plays a dominant role in dictating the model output. It is not influenced significantly by the other input features. A mixed trend is observed for both cell angle and vertical cell length. These parameters increase or decrease the model output for low Poisson's ratio configurations. Such a mixed trend indicates that other input features significantly influence the model output for both cell angle and vertical cell length in the model. The trend concerning cell thickness also shows a mixed response. However, the overall variations are relatively narrow. The model output hovers around the expected mean value for changes in cell thickness. Overall, in this study, both SHAP violin and SHAP riverflow plots were implemented to explain the impact and relevance of geometrical features on Poisson's ratios and vice versa. SHAP violin allowed for the identification of the key geometrical features that influenced the prediction of Poisson's ratios, while SHAP river flow explored the influence of different input features on each Poisson's ratio. Thus, synergistic implementation of these two metrics facilitates a comprehensive understanding of the behavior of the NN model and its relationship with the input features. This study primarily focused on the linear elastic response under small displacements, where a constant Poisson's ratio was assumed. It should be noted, however, that under large deformations, the evaluation of strain-dependent Poisson's ratios may be necessary, presenting an interesting avenue for future research.

4. Conclusion

This paper presents an ML-based technique to predict the auxetic response of 3D-printed re-entrant honeycomb TPU non-self-intersecting structures. Upon completion of this study, the findings are as follows.

- The dataset obtained using the experimentally validated FEA model can be used to successfully develop a predictive model for the auxetic behavior of re-entrant honeycomb TPU structures using feed-forward MLP and back propagation NN algorithms where two hidden layers and five neurons at each level of the hidden layer are found to be the optimum hyperparameters during tuning.
- The SHAP values suggest that slant cell length has the highest influence on the prediction of the Poisson's ratio, followed by the cell angle, the vertical cell length, and the cell thickness.
- The SHAP river flow plot shows that slant cell length is an independent dominant input feature that dictates the model output values. In contrast, cell angle and vertical cell length show mixed trends signifying that other input features influence their effect on the model output.

- The results also show that the cell thickness does not significantly influence the model output when compared to other input features.

Overall, the results presented in this study establish an ML tool to predict the auxetic behavior of 3D-printed re-entrant honeycomb TPU structures with custom geometrical properties to assist the materials engineers and researchers in making informed materials and design decisions. Moreover, the integration of the developed ML model with traditional topology or phase optimization methods offers a promising future research direction for efficient and innovative re-entrant honeycomb structure design. The ML model can be used as an efficient surrogate model during the optimization process. The optimization algorithm can leverage the model's predictions to guide the search for optimal geometries and material layouts, reducing the computational burden typically associated with iterative numerical simulations or the number of experiments. This integrated approach enables a broader exploration of the design space, more accurate performance predictions, and the discovery of novel geometries with enhanced mechanical properties or unique behavior for various functional negative Poisson's ratio applications, opening up a promising avenue for future research. The method in this study applies to recurring re-entrant honeycomb units but can also be extended to other auxetic metamaterials with re-entrant units such as the lozenge, rotating triangle, chiral, double arrow, rotating rectangle, star, and S-structure.

Credit author statement

Bolaji Oladipo: Software, Validation, Formal analysis, Investigation, Data Curation, Writing - Original Draft, Visualization. **Helio Matos:** Validation, Investigation, Writing - Review & Editing. **N M Anoop Krishnan:** Methodology, Software, Writing - Review & Editing. **Sumanta Das:** Conceptualization, Methodology, Resources, Writing - Review & Editing, Supervision, Project administration, Funding acquisition.

Data availability

The raw data required to reproduce these findings are available to download from <https://doi.org/10.17632/3wxyzfvyh6.1>.

Declaration of competing interest

The authors declare that they have no known competing financial interests or personal relationships that could have appeared to influence the work reported in this paper.

Acknowledgment

Funding for this research is provided by the Transportation Infrastructure Durability Center at the University of Maine

under grant 69A3551847101 from the U.S. Department of Transportation's University Transportation Centers Program. This research was conducted in the Multiscale & Multiphysics Mechanics Laboratory at the University of Rhode Island, and the supports that have made this laboratory possible are acknowledged. The authors acknowledge Bluewaves and Andromeda High-Performance Research Computing at the University of Rhode Island (URI) for providing computer clusters and data storage resources that have contributed to the research results reported in this paper.

Appendix A. Supplementary data

Supplementary data to this article can be found online at <https://doi.org/10.1016/j.jmr.2023.06.038>.

REFERENCES

- [1] Jiang Y, Li Y. 3D printed auxetic mechanical metamaterial with chiral cells and Re-entrant cores. *Sci Rep* 2018;8:2397. <https://doi.org/10.1038/s41598-018-20795-2>.
- [2] Ren X, Das R, Tran P, Ngo TD, Xie YM. Auxetic metamaterials and structures: a review. *SMS* 2018;27:23001. <https://doi.org/10.1088/1361-665X/aaa61c>.
- [3] Su Y, Wu X, Shi J. A novel 3D printable multimaterial auxetic metamaterial with reinforced structure: improved stiffness and retained auxetic behavior. *Mech Adv Mater Struct* 2022;29:408–18. <https://doi.org/10.1080/15376494.2020.1774690>.
- [4] Novak N, Hokamoto K, Vesenjak M, Ren Z. Mechanical behaviour of auxetic cellular structures built from inverted tetrapods at high strain rates. *Int J Impact Eng* 2018;122:83–90. <https://doi.org/10.1016/j.ijimpeng.2018.08.001>.
- [5] Lakes R. Foam structures with a negative Poisson's ratio. *Science* 1987;235:1038–40.
- [6] Shen L, Wang X, Li Z, Wei K, Wang Z. Elastic properties of an additive manufactured three-dimensional vertex-based hierarchical re-entrant structure. *Mater Des* 2022;216:110527. <https://doi.org/10.1016/j.matdes.2022.110527>.
- [7] Lyngdoh GA, Kelter N-K, Doner S, Krishnan NMA, Das S. Elucidating the auxetic behavior of cementitious cellular composites using finite element analysis and interpretable machine learning. *Mater Des* 2022;213:110341. <https://doi.org/10.1016/j.matdes.2021.110341>.
- [8] Li Z-Y, Wang X-T, Ma L, Wu L-Z. Study on the mechanical properties of CFRP composite auxetic structures consist of corrugated sheets and tubes. *Compos Struct* 2022;292:115655. <https://doi.org/10.1016/j.compstruct.2022.115655>.
- [9] Borovinšek M, Novak N, Vesenjak M, Ren Z, Ulbin M. Designing 2D auxetic structures using multi-objective topology optimization. *Mater Sci Eng, A* 2020;795:139914. <https://doi.org/10.1016/j.msea.2020.139914>.
- [10] Bhullar SK, Ko J, Cho Y, Jun MBG. Fabrication and characterization of nonwoven auxetic polymer stent. *Null* 2015;54:1553–9. <https://doi.org/10.1080/03602559.2014.986812>.
- [11] Greaves GN, Greer AL, Lakes RS, Rouxel T. Poisson's ratio and modern materials. *Nat Mater* 2011;10:823–37. <https://doi.org/10.1038/nmat3134>.
- [12] Dudek KK, Gatt R, Dudek MR, Grima JN. Negative and positive stiffness in auxetic magneto-mechanical metamaterials.

- Proc R Soc A 2018;474:20180003. <https://doi.org/10.1098/rspa.2018.0003>.
- [13] Zheng Xiaoyu, Lee Howon, Weisgraber Todd H, Maxim Shusteff, Joshua DeOtte, Duoss Eric B, et al. Ultralight, ultrastiff mechanical metamaterials. *Science* 2014;344:1373–7. <https://doi.org/10.1126/science.1252291>.
 - [14] Namvar N, Ali Z, Vakili-Tahami F, Bodaghi Mahdi. Reversible energy absorption of elasto-plastic auxetic, hexagonal, and AuxHex structures fabricated by FDM 4D printing. *Smart materials and structures*. 2022.
 - [15] Donoghue JP, Alderson KL, Evans KE. The fracture toughness of composite laminates with a negative Poisson's ratio. *Physica Status Solidi (B) Basic Research* 2009;246:2011. <https://doi.org/10.1002/pssb.200982031>.
 - [16] Zhang J, Lu G, Ruan D, Wang Z. Tensile behavior of an auxetic structure: analytical modeling and finite element analysis. *Int J Mech Sci* 2018;136:143–54. <https://doi.org/10.1016/j.jimecs.2017.12.029>.
 - [17] Tomažinčič D, Nečemer B, Vesenjak M, Klemenc J. Low-cycle fatigue life of thin-plate auxetic cellular structures made from aluminium alloy 7075-T651. *Fatig Fract Eng Mater Struct* 2019;42:1022–36. <https://doi.org/10.1111/ffe.12966>.
 - [18] Jin Y, Xie C, Gao Q, Zhou X, Li G, Du J, et al. Fabrication of multi-scale and tunable auxetic scaffolds for tissue engineering. *Mater Des* 2021;197:109277. <https://doi.org/10.1016/j.matdes.2020.109277>.
 - [19] Shukla S, Behera BK. Auxetic fibrous structures and their composites: a review. *Compos Struct* 2022;290:115530. <https://doi.org/10.1016/j.compstruct.2022.115530>.
 - [20] Ali M, Zeeshan M, Qadir MB, Riaz R, Ahmad S, Nawab Y, et al. Development and mechanical characterization of weave design based 2D woven auxetic fabrics for protective textiles. *Fibers Polym* 2018;19:2431–8. <https://doi.org/10.1007/s12221-018-8627-8>.
 - [21] Smardzewski J, Kłos R, Fabisiak B. Design of small auxetic springs for furniture. *Mater Des* 2013;51:723–8. <https://doi.org/10.1016/j.matdes.2013.04.075>.
 - [22] Kim E, Zhang H, Lee J-H, Chen H, Zhang H, Javed MH, et al. MXene/polyurethane auxetic composite foam for electromagnetic interference shielding and impact attenuation. *Compos Appl Sci Manuf* 2021;147:106430. <https://doi.org/10.1016/j.compositesa.2021.106430>.
 - [23] Wang S, Deng C, Ojo O, Akinrinlola B, Kozub J, Wu N. Design and modeling of a novel three dimensional auxetic reentrant honeycomb structure for energy absorption. *Compos Struct* 2022;280:114882. <https://doi.org/10.1016/j.compstruct.2021.114882>.
 - [24] Jeong S, Yoo HH. Shape optimization of bowtie-shaped auxetic structures using beam theory. *Compos Struct* 2019;224:111020. <https://doi.org/10.1016/j.compstruct.2019.111020>.
 - [25] Kolken HMA, Zadpoor A. Auxetic mechanical metamaterials. *RSC Adv* 2017;7:5111–29. <https://doi.org/10.1039/C6RA27333E>.
 - [26] Grima JN, Chetcuti E, Manicaro E, Attard D, Camilleri M, Gatt R, et al. On the auxetic properties of generic rotating rigid triangles. *Proc R Soc A* 2012;468:810–30. <https://doi.org/10.1098/rspa.2011.0273>.
 - [27] Günaydın K, Sala G, Türkmen HS, Grande AM. Failure analysis of auxetic lattice structures under crush load. *Procedia Struct Integr* 2022;35:237–46. <https://doi.org/10.1016/j.prostr.2021.12.070>.
 - [28] Johnston R, Kazancı Z. Analysis of additively manufactured (3D printed) dual-material auxetic structures under compression. *Addit Manuf* 2021;38:101783. <https://doi.org/10.1016/j.addma.2020.101783>.
 - [29] Yang W, Huang R, Liu J, Liu J, Huang W. Ballistic impact responses and failure mechanism of composite double-arrow auxetic structure. *Thin-Walled Struct* 2022;174:109087. <https://doi.org/10.1016/j.tws.2022.109087>.
 - [30] Grima J N, Gatt R, Alderson A, Evans K E. On the auxetic properties of 'Rotating rectangles' with different connectivity. *J Phys Soc Jpn* 2005;74:2866–7. <https://doi.org/10.1143/JPSJ.74.2866>.
 - [31] Zhang W-M, Li Z-Y, Yang J-S, Ma L, Lin Z, Schmidt R, et al. A lightweight rotationally arranged auxetic structure with excellent energy absorption performance. *Mech Mater* 2022;166:104244. <https://doi.org/10.1016/j.mechmat.2022.104244>.
 - [32] Meena K, Singamneni S. A new auxetic structure with significantly reduced stress concentration effects. *Mater Des* 2019;173:107779. <https://doi.org/10.1016/j.matdes.2019.107779>.
 - [33] Sun Y, Ye W, Chen Y, Fan W, Feng J, Sareh P. Geometric design classification of kirigami-inspired metastructures and metamaterials. *Structures* 2021;33:3633–43. <https://doi.org/10.1016/j.istruc.2021.06.072>.
 - [34] Lin W, Yang F, Zhang J. A twofold-symmetric kirigami pattern and its mobile tessellations. *Mech Mach Theor* 2022;174:104916. <https://doi.org/10.1016/j.mechmachtheory.2022.104916>.
 - [35] Del Broccolo S, Laurenzi S, Scarpa F. AUXHEX – a Kirigami inspired zero Poisson's ratio cellular structure. *Compos Struct* 2017;176:433–41. <https://doi.org/10.1016/j.compstruct.2017.05.050>.
 - [36] Zhao TF, Deng ZC, Fu CY, Wang XJ, Zhou HY, Chen CQ. Thickness effect on mechanical behavior of auxetic sintered metal fiber sheets. *Mater Des* 2019;167:107635. <https://doi.org/10.1016/j.matdes.2019.107635>.
 - [37] Li Z, Wang KF, Wang BL. Indentation resistance of brittle auxetic structures: combining discrete representation and continuum model. *Eng Fract Mech* 2021;252:107824. <https://doi.org/10.1016/j.engfracmech.2021.107824>.
 - [38] Novak N, Dobnik Dubrovski P, Borovinšek M, Vesenjak M, Ren Z. Deformation behaviour of advanced textile composites with auxetic structure. *Compos Struct* 2020;252:112761. <https://doi.org/10.1016/j.compstruct.2020.112761>.
 - [39] El Dhaba AR, Shaat M. Modeling deformation of auxetic and non-auxetic polymer gels. *Appl Math Model* 2019;74:320–36. <https://doi.org/10.1016/j.apm.2019.04.050>.
 - [40] Lalegani Dezaki M, Serjouei A, Zolfagharian A, Fotouhi M, Moradi M, Ariffin MKA, et al. A review on additive/subtractive hybrid manufacturing of directed energy deposition (DED) process. *Advan Pow Mater* 2022:100054. <https://doi.org/10.1016/j.apmate.2022.100054>.
 - [41] Wang B, Tao F, Fang X, Liu C, Liu Y, Freiheit T. Smart manufacturing and intelligent manufacturing: a comparative review. *Engineering* 2021;7:738–57. <https://doi.org/10.1016/j.eng.2020.07.017>.
 - [42] Zhang J, Lu G, You Z. Large deformation and energy absorption of additively manufactured auxetic materials and structures: a review. *Compos B Eng* 2020;201:108340. <https://doi.org/10.1016/j.compositesb.2020.108340>.
 - [43] Meena K, Singamneni S. Novel hybrid auxetic structures for improved in-plane mechanical properties via additive manufacturing. *Mech Mater* 2021;158:103890. <https://doi.org/10.1016/j.mechmat.2021.103890>.
 - [44] Li B, Zhang S, Zhang L, Gao Y, Xuan F. Strain sensing behavior of FDM 3D printed carbon black filled TPU with periodic configurations and flexible substrates. *J Manuf Process* 2022;74:283–95. <https://doi.org/10.1016/j.jmapro.2021.12.020>.

- [45] Van Waelegheem T, Marchesini FH, Cardon L, D'hooge DR. Melt exit flow modelling and experimental validation for fused filament fabrication: from Newtonian to non-Newtonian effects. *J Manuf Process* 2022;77:138–50. <https://doi.org/10.1016/j.jmapro.2022.03.002>.
- [46] Liu J, Ye J, Momin F, Zhang X, Li A. Nonparametric Bayesian framework for material and process optimization with nanocomposite fused filament fabrication. *Addit Manuf* 2022;54:102765. <https://doi.org/10.1016/j.addma.2022.102765>.
- [47] González-Henríquez CM, Sarabia-Vallejos MA, Rodríguez-Hernández J. Polymers for additive manufacturing and 4D-printing: materials, methodologies, and biomedical applications. *Prog Polym Sci* 2019;94:57–116. <https://doi.org/10.1016/j.progpolymsci.2019.03.001>.
- [48] Rimašauskas M, Jasiūnienė E, Kuncius T, Rimašauskienė R, Cicenė V. Investigation of influence of printing parameters on the quality of 3D printed composite structures. *Compos Struct* 2022;281:115061. <https://doi.org/10.1016/j.compstruct.2021.115061>.
- [49] Photiou D, Avraam S, Sillani F, Verga F, Jay O, Papadakis L. Experimental and numerical analysis of 3D printed polymer tetra-petal auxetic structures under compression. *Appl Sci* 2021;11. <https://doi.org/10.3390/app112110362>.
- [50] Li B, Liang W, Zhang L, Ren F, Xuan F. TPU/CNTs flexible strain sensor with auxetic structure via a novel hybrid manufacturing process of fused deposition modeling 3D printing and ultrasonic cavitation-enabled treatment. *Sensor Actuatur Phys* 2022;340:113526. <https://doi.org/10.1016/j.sna.2022.113526>.
- [51] Huang X, Panahi-Sarmad M, Dong K, Cui Z, Zhang K, Gelis Gonzalez O, et al. 4D printed TPU/PLA/CNT wave structural composite with intelligent thermal-induced shape memory effect and synergistically enhanced mechanical properties. *Compos Appl Sci Manuf* 2022:106946. <https://doi.org/10.1016/j.compositesa.2022.106946>.
- [52] Rodríguez-Parada L, de la Rosa S, Mayuet PF. Influence of 3D-printed TPU properties for the design of elastic products. *Polymers* 2021;13:2519. <https://doi.org/10.3390/polym13152519>.
- [53] Li Z, Wang Z, Gan X, Fu D, Fei G, Xia H. Selective laser sintering 3D printing: a way to construct 3D electrically conductive segregated network in polymer matrix. *Macromol Mater Eng* 2017;302:1700211. <https://doi.org/10.1002/mame.201700211>.
- [54] Haryńska A, Gubanska I, Kucinska-Lipka J, Janik H. Fabrication and characterization of flexible medical-grade TPU filament for fused deposition modeling 3DP technology. *Polymers* 2018;10. <https://doi.org/10.3390/polym10121304>.
- [55] Dong K, Panahi-Sarmad M, Cui Z, Huang X, Xiao X. Electro-induced shape memory effect of 4D printed auxetic composite using PLA/TPU/CNT filament embedded synergistically with continuous carbon fiber: a theoretical & experimental analysis. *Compos B Eng* 2021;220:108994. <https://doi.org/10.1016/j.compositesb.2021.108994>.
- [56] Tabuani D, Bellucci F, Terenzi A, Camino G. Flame retarded Thermoplastic Polyurethane (TPU) for cable jacketing application. *Polym Degrad Stab* 2012;97:2594–601. <https://doi.org/10.1016/j.polymdegradstab.2012.07.011>.
- [57] Lang JP, Jiang W, Teng XC, Zhang XG, Han D, Hao J, et al. Assembled mechanical metamaterials with transformable shape and auxeticity. *Construct Build Mater* 2023;378:131181. <https://doi.org/10.1016/j.conbuildmat.2023.131181>.
- [58] Jiang W, Zhang XG, Han D, Wang L, Chen WQ, Xie YM, et al. Experimental and numerical analysis of a novel assembled auxetic structure with two-stage programmable mechanical properties. *Thin-Walled Struct* 2023;185:110555. <https://doi.org/10.1016/j.tws.2023.110555>.
- [59] Zhang Y, Ren X, Jiang W, Han D, Yu Zhang X, Pan Y, et al. In-plane compressive properties of assembled auxetic chiral honeycomb composed of slotted wave plate. *Mater Des* 2022;221:110956. <https://doi.org/10.1016/j.matdes.2022.110956>.
- [60] Zhang XY, Ren X, Zhang Y, Xie YM. A novel auxetic metamaterial with enhanced mechanical properties and tunable auxeticity. *Thin-Walled Struct* 2022;174:109162. <https://doi.org/10.1016/j.tws.2022.109162>.
- [61] Gao Q, Ding Z, Liao W-H. Effective elastic properties of irregular auxetic structures. *Compos Struct* 2022;287:115269. <https://doi.org/10.1016/j.compstruct.2022.115269>.
- [62] Wang T, Xie Y, Wang L, Zhang X, Ma Z. Size effects of elastic properties for auxetic cellular structures: bending energy-based method. *Mater Today Commun* 2022;31:103585. <https://doi.org/10.1016/j.mtcomm.2022.103585>.
- [63] Vadyala SR, Betgeri SN, Matthews JC, Matthews E. A review of physics-based machine learning in civil engineering. *Results Eng* 2022;13:100316. <https://doi.org/10.1016/j.rineng.2021.100316>.
- [64] Oladipo B, Ajide OO, Monyei C. Corrosion assessment of some buried metal pipes using neural network algorithm. *Inter J Eng Manufac* 2017;7:27–42. <https://doi.org/10.5815/ijem.2017.06.03>.
- [65] Pan Y, Stark R. An interpretable machine learning approach for engineering change management decision support in automotive industry. *Comput Ind* 2022;138:103633. <https://doi.org/10.1016/j.compind.2022.103633>.
- [66] Thai H-T. Machine learning for structural engineering: a state-of-the-art review. *Structures* 2022;38:448–91. <https://doi.org/10.1016/j.istruc.2022.02.003>.
- [67] Zhilyaev I, Krushinsky D, Ranjbar M, Krushynska AO. Hybrid machine-learning and finite-element design for flexible metamaterial wings. *Mater Des* 2022;218:110709. <https://doi.org/10.1016/j.matdes.2022.110709>.
- [68] Xu M, Zhao Z, Wang P, Duan S, Lei H, Fang D. Mechanical performance of bio-inspired hierarchical honeycomb metamaterials. *Int J Solid Struct* 2022;254–255:111866. <https://doi.org/10.1016/j.ijsolstr.2022.111866>.
- [69] Zeng W, Jiang W, Liu J, Huang W. Fabrication method and dynamic responses of composite sandwich structure with reentrant honeycomb cores. *Compos Struct* 2022;299:116084. <https://doi.org/10.1016/j.compstruct.2022.116084>.
- [70] Liu Z, Liu J, Liu J, Zeng W, Huang W. The impact responses and failure mechanism of composite gradient reentrant honeycomb structure. *Thin-Walled Struct* 2023;182:110228. <https://doi.org/10.1016/j.tws.2022.110228>.
- [71] Jiang W, Zhou J, Liu J, Zhang M, Huang W. Free vibration behaviours of composite sandwich plates with reentrant honeycomb cores. *Appl Math Model* 2023;116:547–68. <https://doi.org/10.1016/j.apm.2022.12.004>.
- [72] Areias P, Rabczuk T, César de Sá J. A finite strain quadrilateral based on least-squares assumed strains. *Eng Struct* 2015;100:1–16. <https://doi.org/10.1016/j.engstruct.2015.05.035>.
- [73] GitHub: Sample Abaqus files: FEA-based numerical evaluation of auxetic response for re-entrant metamaterials. <https://github.com/bolaji1/Sample-Abaqus-files-FEA-based-numerical-evaluation-of-auxetic-response-for-reentrant-metamaterials>.
- [74] Zouaoui M, Gardan J, Lafon P, Labergere C, Makke A, Recho N. Transverse isotropic behavior identification using digital image correlation of a pre-structured material manufactured by 3D printing. *Procedia Struct Integr* 2020;28:978–85. <https://doi.org/10.1016/j.prostr.2020.11.112>.
- [75] Uddin KZ, Pagliocca N, Anni IA, Youssef G, Koohbor B. Multiscale strain field characterization in flexible planar

- auxetic metamaterials with rotating squares. *Adv Eng Mater* 2022. <https://doi.org/10.1002/adem.202201248>. n/a:2201248.
- [76] Columbia, SC, USA VIC-2D manual, correlated solutions. 2009. <https://correlated.kayako.com/article/86-vic-2d-7-manual>.
- [77] Pan L, Novák L, Lehký D, Novák D, Cao M. Neural network ensemble-based sensitivity analysis in structural engineering: comparison of selected methods and the influence of statistical correlation. *Comput Struct* 2021;242:106376. <https://doi.org/10.1016/j.compstruc.2020.106376>.
- [78] Chen C, Min F, Zhang Y, Bao H. ReLU-type Hopfield neural network with analog hardware implementation. *Chaos, Solit Fractals* 2023;167:113068. <https://doi.org/10.1016/j.chaos.2022.113068>.
- [79] Kingma DP, Ba J. Adam: a method for stochastic optimization. 3rd international conference on learning representations, ICLR 2015. San Diego, CA, USA: Conference Track Proceedings; 2015. May 7-9, 2015.
- [80] Abadi M, Barham P, Chen J, Chen Z, Davis A, Dean J, et al. TensorFlow: a system for large-scale machine learning. 2016.
- [81] Naji MA, Filali SE, Aarika K, Benlahmar EH, Abdelouahid RA, Debauche O. Machine learning algorithms for breast cancer prediction and diagnosis. *Proc Comput Sci* 2021;191:487–92. <https://doi.org/10.1016/j.procs.2021.07.062>.
- [82] Cawley GC, Talbot NLC. On over-fitting in model selection and subsequent selection bias in performance evaluation. *J Mach Learn Res* 2010;11:2079–107.
- [83] Yang K, Xu X, Yang B, Cook B, Ramos H, Krishnan NMA, et al. Predicting the young's modulus of silicate glasses using high-throughput molecular dynamics simulations and machine learning. *Sci Rep* 2019;9:8739. <https://doi.org/10.1038/s41598-019-45344-3>.
- [84] Mangalathu S, Karthikeyan K, Feng D-C, Jeon J-S. Machine-learning interpretability techniques for seismic performance assessment of infrastructure systems. *Eng Struct* 2022;250:112883. <https://doi.org/10.1016/j.engstruct.2021.112883>.
- [85] Bhattoo R, Bishnoi S, Zaki M, Krishnan NMA. Revealing the compositional control of electrical, mechanical, optical, and physical properties of inorganic glasses. 2021.